10. M. Rottmann *et al.*, *Science* **329**, 1175 (2010).
11. G. J. Crowther *et al.*, *Mol. Biochem. Parasitol.* **175**, 21 (2011).
12. K. Gagaring *et al.*, Novartis-GNF Malaria Box, in *ChEMBL-NTD*, www.ebi.ac.uk/chemblntd (2010).
13. S. F. Yan, H. Asatryan, J. Li, Y. Zhou, *J. Chem. Inf. Model.* **45**, 1784 (2005).
14. P. Wang, M. Read, P. F. Sims, J. E. Hyde, *Mol. Microbiol.* **23**, 979 (1997).
15. P. Wang, N. Nirmalan, Q. Wang, P. F. Sims, J. E. Hyde, *Mol. Biochem. Parasitol.* **135**, 77 (2004).
16. T. Wu *et al.*, *J. Med. Chem.* **54**, 5116 (2011).
17. S. Yalaoui *et al.*, *PLoS Pathog.* **4**, e1000010 (2008).
18. H. J. Painter, J. M. Morrisey, M. W. Mather, A. B. Vaidya, *Nature* **446**, 88 (2007).
19. T.-G. Nam *et al.*, *ACS Chem. Biol.* 110908113621066 (2011).
20. I. Maeda, Y. Kohara, M. Yamamoto, A. Sugimoto, *Curr. Biol.* **11**, 171 (2001).
21. E. A. Winzeler *et al.*, *Science* **285**, 901 (1999).
22. M. C. Jonikas *et al.*, *Science* **323**, 1693 (2009).
23. C. Aurrecoechea *et al.*, *Nucleic Acids Res.* **37**, D539 (2008).
24. D. Mazier, L. Rénia, G. Snounou, *Nat. Rev. Drug Discov.* **8**, 854 (2009).
25. Y. Dong *et al.*, *J. Med. Chem.* **53**, 481 (2010).
26. S. A. Charman *et al.*, *Proc. Natl. Acad. Sci. U.S.A.* **108**, 4400 (2011).
27. D. E. Davidson Jr. *et al.*, *Bull. World Health Organ.* **59**, 463 (1981).
28. E. S. Istvan *et al.*, *Proc. Natl. Acad. Sci. U.S.A.* **108**, 1627 (2011).
29. N. V. Dharia *et al.*, *Genome Biol.* **10**, R21 (2009).
30. D. M. Plouffe *et al.*, *Proc. Natl. Acad. Sci. U.S.A.* **105**, 9059 (2008).

Acknowledgments: We wish to thank I. Sherman for helpful comments on the manuscript, members of the New York University Insectary for providing infected mosquitoes and C. Fischli for *P. berghei* efficacy testing. The whole genome sequencing data has been deposited at the National Center for Biotechnology Information (NCBI) Sequence Read Archive database (http://trace.ncbi.nlm.nih.gov/Traces/sra/sra.cgi?) with the project accession no. SRA045972.1. The microarray data has been deposited at the NCBI Gene Expression Omnibus database (www.ncbi.nlm.nih.gov/geo/) with the accession no. GSE32485. The assay data was deposited at the ChEMBL–Neglected Tropical Disease (ChEMBL-NTD) archive (www.ebi.ac.uk/chemblntd/) with the accession nos. CHEMBL1789904, CHEMBL1789905, and CHEMBL1789906. E.A.W. is supported by the Keck Foundation and by the NIH (grant R01AI090141). S.M. was supported by Deutsche Forschungsgemeinschaft (ME 3528/1-1). Funding for M.C.S.L. and D.A.F. is provided in part by the Medicines for Malaria Venture and the NIH (grant R01 AI079709). We gratefully acknowledge translational research support (WT078285) from the Wellcome Trust and funding from the Medicines for Malaria Venture to the Genomics Institute of the Novartis Research Foundation, the Swiss Tropical and Public Health Institute, and the Novartis Institute for Tropical Diseases. All compounds disclosed are either commercially available from compound vendors (vendor identifications can be sourced from the ChEmbl database), or, if members of the imidazolopiperazine series are required, they will be provided by materials transfer agreement. A materials transfer agreement will be provided by P. Froissard and INSERM-UMR945 for requests for the HepG2-CD81-eGFP cell line.

Supporting Online Material

www.sciencemag.org/cgi/content/full/science.1211936/DC1
Materials and Methods
Tables S1 to S13
Figs. S1 to S5
References (*32*–*61*)

29 July 2011; accepted 6 October 2011
Published online 17 November 2011;
10.1126/science.1211936

Carving at the Nanoscale: Sequential Galvanic Exchange and Kirkendall Growth at Room Temperature

Edgar González,[1,2]* Jordi Arbiol,[3,4] Víctor F. Puntes[1,2,4,5]†

Shape control of inorganic nanocrystals is important for understanding basic size- and shape-dependent scaling laws and is useful in a wide range of applications. With minor modifications in the chemical environment, it is possible to control the reaction and diffusion processes at room temperature, opening up a synthetic route for the production of polymetallic hollow nanoparticles with very different morphology and composition, obtained by the simultaneous or sequential action of galvanic replacement and the Kirkendall effect.

We use molecular reducing agents and coordinating complexes to facilitate combined galvanic exchange and Kirkendall growth at room temperature to produce very unique structures of high complexity, in a context where structure determines properties. These structures, from monodisperse single- and double-walled open nanoboxes to noble metal fullerenes-like nanoparticles (NPs), are produced in a simple manner at room temperature, in the aqueous phase, in high yields, with a large-scalable synthesis (fig. S1).

The production of metallic hollow NPs, either by galvanic replacement (*1*) or by the Kirkendall effect (*2*), requires high temperatures to ensure structures with soft surfaces and well-defined morphology (*3*, *4*). Protocols at lower temperatures would require an increase of the diffusion coefficient to favor mobility of vacancies and jumps of atoms in the crystal and dissolution of the compounds with low solubility formed during the oxidation process. Both of these are important problems because of their influence on the crystallization of metallic surfaces, specifically epitaxial growth (*3*). This is fundamental for the appealing applications of hollow NPs in many areas of science and technology—such as catalysis (*5*), plasmonics (*6*), bioencapsulation (*7*), drug delivery (*8*, *9*), and nanoelectronics (*10*)—where they are excellent benchworks. The interest in developing this kind of nanostructures continues to today, as reflected in more recent literature (*11*–*16*).

By using silver as template; polyvinylpyrrolidone (PVP) as surfactant; cetyl trimethylammonium bromide (CTAB) as surfactant and complexing agent; gold, palladium, and platinum as oxidizing agents; and ascorbic acid as reducing agent; nanoparticles with different levels of structural hierarchy were easily obtained at room temperature. In the presence of CTAB, ascorbic acid reduces $AuCl_4^-$ to $AuCl_2^-$ (*17*), decreasing its lability and allowing Kirkendall effect to take place. Furthermore, it solubilizes AgBr and AgCl formed upon oxidation of silver (*18*) (also fig. S2). A detailed explanation on the synthetic procedures is given in the Materials and Methods section of the supporting online material (SOM).

As an example, Fig. 1 shows concentric double-walled nanoboxes. When the reaction begins, oxidation of silver provides one electron to reduce one gold ion. Because gold and silver have the same face-centered cubic (fcc) structure and about equal lattice constants, gold atoms are epitaxially deposited onto the silver surface as a thin layer (Fig. 1A2). The covering of Ag with Au protects Ag from oxidation. As the relative area of the electrodes increases, corrosion becomes progressively stronger at the uncovered areas, which leads to the formation of pinholes, from which the silver cube is emptied. A galvanic reaction follows between the Ag inner electrode and the Au outer one, in which the pitting site serves as the anode where the silver is oxidized and its electrons are stripped. The released electrons can easily migrate to the surface of the nanocube and are captured by $AuCl^-_2$ ions to generate gold atoms that preferentially nucleate and grow on the surface of the template (Fig. 1A4). The dissolution of Ag^+ ions increases the local concentrations of Br^- and Cl^-, favoring pit growth by autocatalytic processes (*19*). As the

[1]Institut Català de Nanotecnologia (ICN), Campus UAB, 08193 Bellaterra, Spain. [2]Universitat Autònoma de Barcelona (UAB), Campus UAB, 08193 Bellaterra, Spain. [3]Institut de Ciència de Materials de Barcelona (ICMAB-CSIC), Campus UAB, 08193 Bellaterra, Spain. [4]Institució Catalana de Recerca i Estudis Avançats (ICREA), Passeig Lluís Companys, 23, 08010 Barcelona, Spain. [5]Centre d'Investigacions en Nanociència i Nanotecnologia CIN2 (ICN-CSIC), Campus UAB, 08193 Bellaterra, Spain.

*Present address: Sección de Nanociencia y Nanotecnología, Instituto Geofísico, Pontificia Universidad Javeriana, 110231 Bogotá, Colombia.

†To whom correspondence should be addressed. E-mail: victor.puntes@icn.cat

ratio between the anode and cathode areas becomes lower with increasing void size, there is a consequent decrease in corrosion rate. Throughout the whole process, the pinhole remains open. Once the cavity is formed by galvanic replacement and its surface covered by a gold layer, the wall can be modeled as a thin film of silver between two layers of gold that forms a diffusion intermetallic coupling, which allows formation of

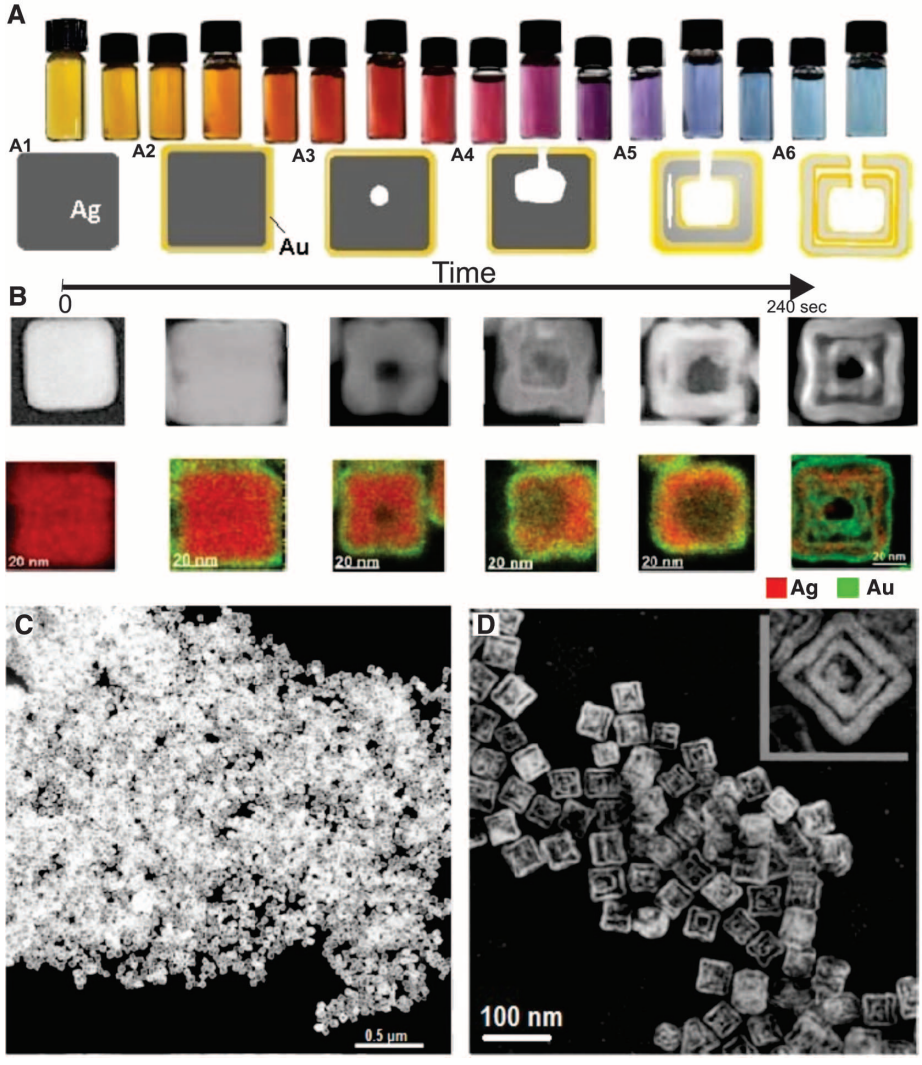

Fig. 1. (**A**) Optical and morphological evolution of AuAg double-walled nanoboxes. (**B**) High-angle annular dark field (HAADF) STEM (Z-contrast) images and EDX maps for the different stages of evolution indicated in (A). (**C** and **D**) TEM images of AuAg double-walled nanoboxes, showing large yield production and the double-walled morphology.

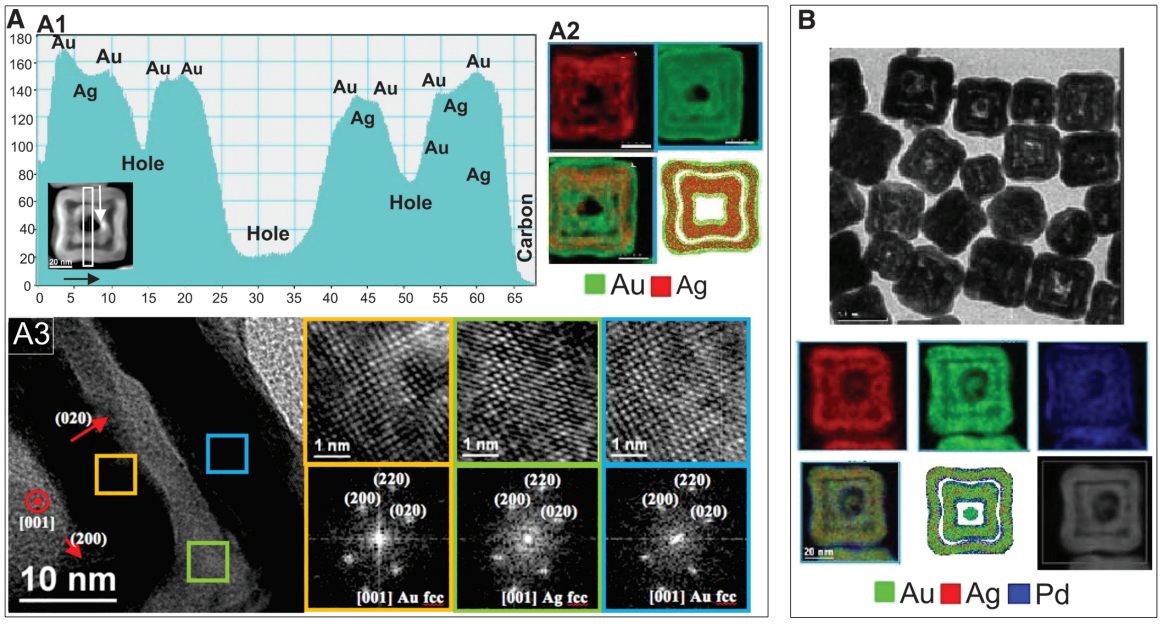

Fig. 2. (**A**) Characterization of double-walled nanoboxes. (**A1**) Intensity profile obtained on the Z-contrast image (inset) of AuAg double-walled nanoboxes. (**A2**) EDX elemental map and elemental distribution scheme. (**A3**) HRTEM characterization. (**B**) TEM image and EDX elemental maps for trimetallic PdAuAg nanoboxes. Palladium is added after gold.

Kirkendall cavities beneath the cube's surface while it continues to be emptied by galvanic replacement. The diffusion of silver in gold is faster than that of gold in silver (*3*); therefore, the difference between fluxes of gold and silver will produce a net flux of vacancies from the surface to the center (Fig. 1A5). Vacancy concentration increases to the point of insolubility, and void bubbles nucleate beneath the surface. These voids grow following the metal interface, coalesce, and form a continuous cavity parallel to the cube surface that eventually drills into the pinhole, which allows the inner walls to be plated with gold. In the reported conditions, double-walled structures are obtained at times greater than 10 min after adding the gold salt. To calculate the approximate formation time, Einstein's equation can be used: $\tau \cong s^2/D$, where s corresponds to 4 nm (distance between the center of the wall and the surface), and D, the diffusion coefficient at room temperature, is 10^{-19} to 10^{-20} m^2/s, which is extraordinarily high (10^{-24} in bulk) (*3*, *4*) (see further details in "Calculation of the diffusion times" in the SOM text). This equation gives a time about equal to 1.6×10^3 s = 27 min, which is relatively close to the observed values. During this process, the initial yellow-colored solution changes toward blue through a range of orange, red, purple, and violet colors (Fig. 1). At the end of this process, the cube edge has grown by 15% (fig. S3).

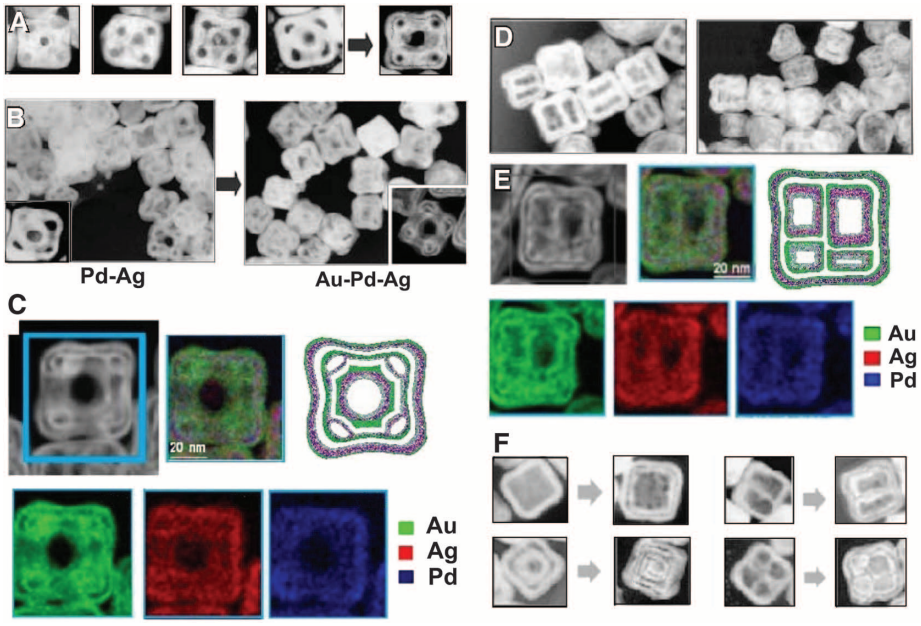

Fig. 3. (**A**) TEM images illustrating the stages of formation of hollow nanostructures by sequential action of galvanic replacement and Kirkendall effect. (**B**) TEM images showing the nanostructures dominated by galvanic replacement using palladium (left) and by Kirkendall effect using gold (right). (**C**) HAADF-STEM image and corresponding EDX elemental maps. (**D**) TEM images of multichambered NPs. (**E**) HAADF-STEM detail and corresponding EDX elemental maps. (**F**) TEM images of different structures produced by sequential action of galvanic replacement and Kirkendall effect.

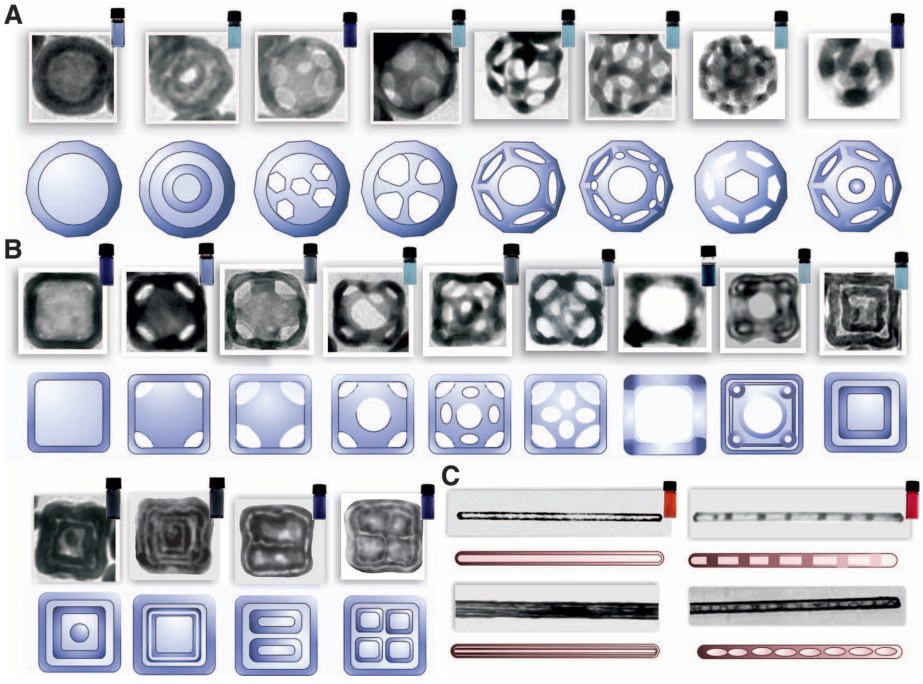

Fig. 4. The synthetic route reported in this work produces structures with (**A**) spherical, (**B**) cubic, and (**C**) cylindrical topologies. TEM images are accompanied by drawings that represent the morphology of each nanostructure.

Diffusion processes are enhanced in NPs (*20*, *21*). This can be sustained on the basis of the following: (i) the large volume fraction of the interfaces formed in these structures, which provides short-circuit diffusion paths; (ii) a high density of defects, such as grain boundaries and vacancies caused by the galvanic replacement; (iii) existence of driving forces, for example, stress fields and dislocations in the crystal that may introduce fast diffusion paths (*22*); and (iv) defects originating from the curvature of surfaces and by replacement of the capping agents. The Br^- that forms AgBr and is deposited at the surface of the template (*3*, *23*) can also play an important role in these considerations.

Energy-dispersive x-ray (EDX) spectra of the final product indicate the presence of 33% gold and 64% silver. After washing the product, 3% bromine is still observed, likely associated with the surfactant layer (fig. S4). This high Ag percentage does not change when a greater volume of Au^+ is added, which indicates that the reaction has reached an end. An external layer of gold remains in the walls of the final structure, as can be verified in the Z-contrast and EDX maps in Fig. 1B. This external gold layer passivates the formed structure and makes it stable over months. The smoothness of this thin gold layer suggests that it is not formed by simple AuAg dealloying (*10*). With a further increase of Au^{3+}, dealloying does take place, and pores are formed in all surfaces of the boxes; these pores grow in size and eventually produce nanoframes at high gold concentrations. Once the nanoframes are formed, additional amounts of Au^{3+} will result in their fragmentation into solid gold pieces or their evolution toward solid particles. In the first growth stages, an overlap of both the Ag and Au signals can be observed in the EDX map (Fig. 1B). Because of the decreased diffusion of each material at room temperature, it is not surprising that spontaneous alloying (*22*) is partially inhibited favoring the formation of the gold overlayer.

High-resolution transmission electron microscopy (HRTEM) analysis of the Au-Ag nanoboxes shows that they are single crystals crystallized

in the Au-Ag fcc structure. Detailed HRTEM analysis of the nanoboxes shows that there is continuity in the cell parameters when crossing from the inner Au-Ag-Au double wall to the outer Au-Ag-Au wall, likely maintaining the original template crystal orientation. The lateral walls correspond to {010} and {100} facets, whereas the top and bottom walls correspond to {001} (Fig. 2C). Z-contrast scanning TEM (STEM) analysis of a double-walled nanobox, illustrated in Fig. 2A, indicates that the gold is preferentially located at the surfaces of the walls. X-ray diffraction (XRD) analysis confirms this atomic distribution (fig. S5).

The obtained nanoboxes have two novel aspects: On the one hand, a pore always stays open, allowing access to their interior. On the other hand, their atomic metal distribution is different than previously reported (*24*), and the fact that the most noble of the metals is located on the surface of the box provides a substantial advantage. Because of gold's chemical stability and inertness, these nanoparticles are suitable for use in oxidizing and biological environments, whereas the presence of silver in the interior of the walls offers several advantages arising from its excellent thermal and electrical conductivity at the nanoscale.

Trimetallic structures of palladium-gold-silver can be also produced by using the same method. The final product is a double-walled nanobox with a core of silver localized at the center of the walls (Fig. 2B), coated with a PdAu alloy or an Au-Pd layer, depending on whether the addition of the Au and Pd precursors was simultaneous or sequential and on their stoichiometric ratio (Fig. 2B). In the shown boxes, gold and silver form an alloy with a silver-rich inner section, whereas palladium is located preferentially on the surfaces of the walls.

Furthermore, multilevel structures can be obtained with the sequential action of galvanic replacement and diffusive processes. In a similar synthetic protocol, a pattern is first carved with palladium, and then gold is added. The resulting geometric pattern, which is formed by symmetrically distributed cavities, becomes the support for a second carving process, although this time finer (thin enveloping cavities) than the previous round. Because silver has the lowest reduction potential of the metals used, it is used as a sacrificial template, whereas use of the palladium (and platinum) salt as oxidizing agent favors the production of symmetrical and segmented cavities, yielding large populations of monodispersed multichambered NPs.

Initially, in the formation of the binary Pd-Ag structure, the removal of silver is dominated by galvanic replacement, whereas the later formation of gaps around these cavities, when the gold salt is added, is governed by the Kirkendall effect (Fig. 3).

Thus, by manipulating the galvanic process and the Kirkendall effect it is possible to open up a route for synthesis of structures with complex morphologies. A chart with some of the possible structures that can be produced is shown in Fig. 4, each of them with small modifications of the described recipes with different but high yields and monodispersity (tables S1 and S2).

One would expect the nonspherical NPs to yield nonuniform shell thickness because of enhanced reactivity and diffusivity at the corners and edges, but we did not observe this effect. As previously reported with cobalt nanodiscs (*4*), shape was preserved and cavities appeared following the template contour. These results are as if the higher reactivity of corners compensate for the longer distance to the cavity center.

It is remarkable how the recovery of "old" problems, processes, and protocols, once applied on a different scale with current powerful instrumental resources, provides interesting pathways to shape matter at the nanoscale. Kirkendall effect and galvanic, pitting, etching, and dealloying corrosion processes have all been intensively studied in bulk materials for decades. In this work, we have revisited and combined them from a new perspective at the nanoscale, where matter is more reactive and therefore corrosive, and diffusive processes are enhanced, which has finally retrieved this rich new family of complex nanostructures.

References and Notes

1. Y. Sun, Y. Xia, *Science* **298**, 2176 (2002).
2. Y. Yin *et al*., *Science* **304**, 711 (2004).
3. Y. Sun, Y. Xia, *J. Am. Chem. Soc.* **126**, 3892 (2004).
4. Y. Yin, C. K. Erdonmez, A. Cabot, J. Hughes, A. P. Alivisatos, *Adv. Funct. Mater.* **16**, 1389 (2006).
5. S. W. Kim, M. Kim, W. Y. Lee, T. Hyeon, *J. Am. Chem. Soc.* **124**, 7642 (2002).
6. S. J. Oldenburg, R. D. Averitt, S. L. Westcott, N. J. Halas, *Chem. Phys. Lett.* **288**, 243 (1998).
7. S. M. Marinakos *et al*., *J. Am. Chem. Soc.* **121**, 8518 (1999).
8. F. Caruso, R. A. Caruso, H. Mohwald, *Science* **282**, 1111 (1998).
9. S. Hyuk Im, U. Jeong, Y. Xia, *Nat. Mater.* **4**, 671 (2005).
10. J. Erlebacher, M. J. Aziz, A. Karma, N. Dimitrov, K. K. Sieradzki, *Nature* **410**, 450 (2001).
11. S. E. Skrabalak *et al*., *Acc. Chem. Res.* **41**, 1587 (2008).
12. J. Zeng, Q. Zhang, J. Chen, Y. Xia, *Nano Lett.* **10**, 30 (2010).
13. M. S. Yavuz *et al*., *Nat. Mater.* **8**, 935 (2009).
14. J. Chen *et al*., *Nano Lett.* **7**, 1318 (2007).
15. X. W. Lou, L. A. Archer, *Adv. Mater. (Deerfield Beach Fla.)* **20**, 1853 (2008).
16. Q. Zhao, Y. Gao, X. Bai, C. Wu, Y. Xie, *Eur. J. Inorg. Chem.* **2006**, 1643 (2006).
17. J. Pérez-Juste, L. M. Liz-Marzán, S. Carnie, D. Y. C. Chan, P. Mulvaney, *Adv. Funct. Mater.* **14**, 571 (2004).
18. Y. Sun, B. T. Mayers, Y. Xia, *Nano Lett.* **2**, 481 (2002).
19. C. W. Yen, M. A. Mahmoud, M. A. El-Sayed, *J. Phys. Chem. A* **113**, 4340 (2009).
20. G. Guisbiers, L. Buchaillot, *Nanotechnology* **19**, 435701 (2008).
21. D. Das, P. P. Chatterjee, I. Manna, S. K. Pabi, *Scr. Mater.* **41**, 861 (1999).
22. T. Shibata *et al*., *J. Am. Chem. Soc.* **124**, 11989 (2002).
23. Y. Bi, G. Lu, *Nanotechnology* **19**, 275306 (2008).
24. S. E. Skrabalak *et al*., *Acc. Chem. Res.* **41**, 1587 (2008).

Acknowledgments: The authors acknowledge funding from grants 2009 SGR 770, NanoAraCat, XaRMAE, CSD2006-00012, CSD2009_00013, MAT2009-14734-C02-01, MAT2010-15138, 2009 SGR 776, and VALTEC09-2-0085. J.A. acknowledges NanoAraCat funding for the use of advanced (S)TEM facilities at Instituto de Nanociencia de Aragón–Laboratorio de Microscopia Avanzada and A. Ibarra for help on STEM alignment. A patent application related to this work was filed 14 March 2011 (European Union application number EP11158024.7).

Supporting Online Material

www.sciencemag.org/cgi/content/full/334/6061/1377/DC1
Materials and Methods
SOM Text
Figs. S1 to S5
Tables S1 and S2
References (*25*, *26*)

17 August 2011; accepted 31 October 2011
10.1126/science.1212822

The Origin of OB Runaway Stars

Michiko S. Fujii[1,2] and Simon Portegies Zwart[1]*

About 20% of all massive stars in the Milky Way have unusually high velocities, the origin of which has puzzled astronomers for half a century. We argue that these velocities originate from strong gravitational interactions between single stars and binaries in the centers of star clusters. The ejecting binary forms naturally during the collapse of a young (≲1 milion years old) star cluster. This model replicates the key characteristics of OB runaways in our galaxy, and it explains the presence of runaway stars of ≳100 solar masses ($M_\odot$) around young star clusters, such as R136 and Westerlund 2. The high proportion and the distributions in mass and velocity of runaways in the Milky Way are reproduced if the majority of massive stars are born in dense and relatively low-mass (5000 to 10,000 $M_\odot$) clusters.

Most stars in our galaxy have relatively low velocities. However, there is a population of fast-moving stars, called OB runaways (*1*), that have considerably higher space motions of >30 km/s (*2*). The origin of such velocities can be attained in two very distinct ways: A runaway can be launched when its binary companion explodes in a supernova (*3*), or by ejection via a dynamical slingshot (*4*). The relative importance of both mechanisms has remained elusive, mainly because both are associated with young stellar populations, and the high speed of a star is generally observed long after it has moved away from its birthplace.

[1]Leiden Observatory, Leiden University, Post Office. Box 9513, 2300 RA Leiden, Netherlands. [2]Graduate School of Science and Engineering, Kagoshima University, 1-21-35 Korimoto, Kagoshima 890-0065, Japan.

*To whom correspondence should be addressed. E-mail: spz@strw.leidenuniv.nl